Composites: Part A 194 (2025) 108803

Contents lists available at ScienceDirect

Composites Part A

journal homepage: www.elsevier.com/locate/compositesa

Tailoring interlaminar shear and mode-I fracture behavior in fiber-composites via soft self-healing thermoplastic inclusions

Jack S. Turicek [a], Vikita Kamala [b], Kalyana B. Nakshatrala [c], Ghadir Haikal [b,*], Jason F. Patrick [a,b,*]

[a] Department of Mechanical and Aerospace Engineering, North Carolina State University, Raleigh, 27695, NC, USA
[b] Department of Civil, Construction, and Environmental Engineering, North Carolina State University, Raleigh, 27695, NC, USA
[c] Department of Civil and Environmental Engineering, University of Houston, Houston, 77204, TX, USA

GRAPHICAL ABSTRACT

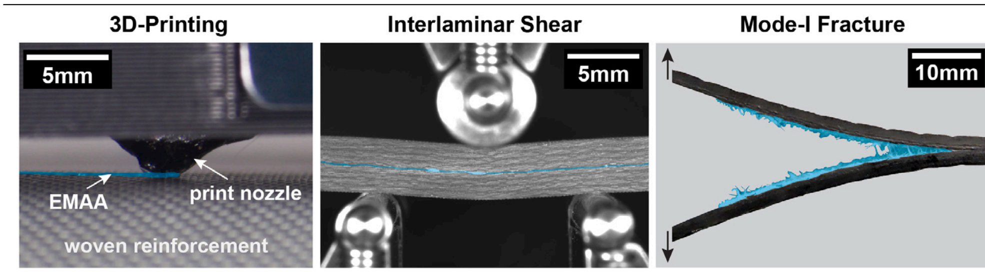

ARTICLE INFO

Keywords:
Self-healing
Mode-I fracture
Interlaminar shear
Finite element modeling
Thermoplastic inclusions

ABSTRACT

The hierarchical microstructure of fiber-reinforced composites (FRC) enables lightweight materials with exceptional mechanical properties. However, their layered architecture is prone to interfacial damage, notably delamination. An effective strategy to mitigate delamination is by integrating thermoplastic interlayers, which not only enhance FRC resistance to interfacial fracture, but also enable self-repair of cracks through thermal mending. In this study, we demonstrate for the first time, repeated *in situ* self-healing of FRC laminates under both mode-I fracture (via the double cantilever beam) and 3-point flexure (employing short-beam shear). Remarkably, we achieve nearly complete restoration over ten consecutive healing cycles from thermal remending of 3D-printed poly(ethylene-co-methacrylic acid) (EMAA) interlayer inclusions. To understand the mechanical effects of such soft inclusions, we conduct a comprehensive experimental and numerical investigation. Our research findings reveal: (i) Markedly different strain states in short-beam shear with soft inclusions compared to FRC without. (ii) The necessity of incorporating contact algorithms for accurate finite element (FE) simulation of local stress/strain fields and global structural responses. (iii) Adjustments in the density and layer placement of printed EMAA domains can tailor both interlaminar shear strength (ILSS) and mode-I fracture resistance (G_{IC}). This research offers newfound insights into realizing self-healing in actual structures, reliable and efficient simulation strategies for modelers, and advancements towards more modern design motifs and suitable materials testing protocols.

* Correspondence to: Fitts-Woolard Hall, 915 Partners Way, North Carolina State University, Raleigh, 27695, NC, USA.
E-mail addresses: ghaikal@ncsu.edu (G. Haikal), jfpatric@ncsu.edu (J.F. Patrick).

https://doi.org/10.1016/j.compositesa.2025.108803
Received 9 October 2024; Received in revised form 29 January 2025; Accepted 11 February 2025
Available online 27 February 2025
1359-835X/© 2025 Elsevier Ltd. All rights are reserved, including those for text and data mining, AI training, and similar technologies.

1. Introduction

Fiber-reinforced composites (FRC) are hierarchical materials engineered to achieve exceptional mechanical properties ideal for lightweight structures. The versatility in FRC architectures allows for tailored properties in high-performance applications, achieved through choices in constituents (matrix/reinforcement), ply orientations, and incorporation of functional elements such as interlayers [1], sensors [2], and vasculature [3]. However, the layered structure of FRC laminates makes them vulnerable to delamination under diverse loading conditions [4]. Delamination manifests in two primary forms: opening (mode-I) fractures occur when tensile loads perpendicular to the fracture plane separate the reinforcement from the matrix [5], while interlaminar shear (mode-II) cracks develop when adjacent layers slide past each other [6]. Detecting and repairing delamination, which typically occurs beneath the surface, poses significant challenges, often requiring extensive structural intervention [7,8]. Left unchecked, delamination can propagate, potentially leading to sudden and catastrophic structural failure.

To mitigate such fatal failures in FRCs, repair strategies based on self-healing have been developed. Because mode-I is the lowest-energy fracture mode in FRC, much contemporary research has focused on improving FRC resilience against this type of delamination. In addition to interlaminar toughening strategies to resist fracture [9–15], the ability to self-heal cracks by different means has been widely studied [16–20]. Extrinsic healing is enabled by incorporating an external healing agent often sequestered inside either embedded capsules [21,22], hollow glass fibers [23–25], or vascular networks [26–29]. When a crack ruptures the respective reservoir, healing agent is released into the damage volume for self-repair via chemical/physical interactions. Conversely, intrinsic healing relies on the reversible nature of a material's chemical bonds, which can reform to heal cracks, provided physical contact is attained. Intrinsic healing is readily achieved in soft polymers at room temperature [30–32]. However, for structural components, an external energy input is often required to obtain mechanically robust bond reformation [33]. Thermal remending is one intrinsic approach where a damaged material self-repairs upon the application of heat and can provide structural restoration within a non-healing host material if effectively placed where damage occurs. Poly(ethylene-co-methacrylic acid) (EMAA) is a popular thermoplastic that exhibits unique chemical reactions when thermally remended in a thermoset epoxy-matrix host [34–36]. Namely, strong interfacial bonding that forms during epoxy cure and the production of water vapor during thermal remending that creates a self-pressurizing micro-porous network forcing the EMAA to fill confined cracks over successive heal cycles [34–47]. Thermal remending has been extensively studied by Mouritz, Varley, and others after incorporating EMAA into fiber-composites by blending with the epoxy matrix [36,39–41], through various types of interlayers (i.e., particles [48], meshes [37,39,46,49], non-woven fabric [38], films [34,35,42]), and fiber stitching/weaving [43–45,50]. Each of these methods have shown the ability to both toughen against mode-I delamination, and self-heal when damage occurs.

Recently, an *in situ* self-healing approach based on thermal remending of 3D printed EMAA in glass and carbon-fiber composites was developed, capable of healing delaminations and recovering fracture properties comparable to those of the virgin material. Notably, this healing process can be repeated up to 100 times, representing an order of magnitude improvement over prior studies [1]. The underlying physical/chemical mechanisms of the healing process have also been furthered [47,51], providing a promising material system platform with *in situ* self-healing capabilities. However, these recent studies primarily focused on healing mode-I fracture in FRCs, raising an important question:

(Q1) Is the approach suitable for a wide range of stress states, loading scenarios, and different fracture modes?

A few prior works revealed that the presence of healable EMAA inclusions caused a significant drop in the interlaminar shear strength (ILSS)—evaluated using a 3-pt flexure "short beam shear" (SBS) test [42,43,46,48] following ASTM D2344. The reduction in ILSS has been attributed to the orders of magnitude difference in ultimate strength between the soft thermoplastic healing agent (≈10 MPa), and the surrounding structural composite (≈400 MPa). The severity of the ILSS decrease compared to a plain composite (i.e., without EMAA inclusions) depended on the method of EMAA incorporation, the location of the inclusions, and the global volume fraction of softer thermoplastic.

Accordingly, we revisit SBS 3-point flexure testing, which due to a short span-to-depth ratio (here 4:1), produces a strong state of shear stress within the fiber-composite alongside bending-induced normal stresses. This complex state of stress interacts with soft EMAA domains, thereby impacting both strength (i.e., ILSS) and stiffness. Stresses in the composite section also deviate from the parabolic distribution of homogeneous isotropic sections assumed by the working beam theory at the core of ASTM D2344, and cannot be easily measured experimentally. It is therefore prudent to establish sound modeling and measurement methods for characterizing the mechanical behavior and self-healing performance of EMAA-modified FRCs. Towards this holistic vision, we first provide sufficient background so one can fully appreciate the intricate and intertwined features of this multifaceted investigation.

In previous studies that heal mode-I fracture, the testing protocol involves: (i) a double cantilever beam (DCB) with *elastic* bending that produces a midplane fracture (i.e., interlaminar delamination); (ii) healing the cracked specimen; (iii) reloading it under the same opening mode-I conditions until fracture. Motivated by the success of this protocol for mode-I, other prior works heal shear-dominated failure following a similar procedure: (i) using a short shear beam and loading in 3-pt bending to failure; (ii) healing the specimen; (iii) reloading the healed SBS specimen again under the same flexural loading conditions. However, a drawback of this adopted approach for SBS is that the mixed-mode stress state results in both healable interfacial fracture but also irreparable fiber breakage, i.e., permanent *inelastic* deformation. Consequently, retesting a deformed SBS specimen via the same 3-pt flexural loading scheme, does not provide the same healed-to-virgin comparison as a mode-I DCB test (per ASTM D5528) where healable damage is confined to a midplane delamination without internal fiber breakage in the composite beams, which (by design) remain mostly elastic.

Thus, in this work, we break from tradition and develop a new SBS healing evaluation protocol (detailed later) where the FRC remains largely elastic and leads to a more precise characterization and clearer understanding of self-recovery in short shear beams. Additionally, the interfacial healing enabled by incorporating discrete domains of the thermally remendable EMAA prompts the following questions:

(Q2) What is the impact of soft EMAA domains on structural integrity?
(Q3) Beyond midplane configurations, what are the optimal locations for EMAA to minimize reductions in mechanical performance while maximizing healing?

Prior structural evaluations of *in situ* self-healing FRC were performed in uniaxial tension [1,51], where the behavior is dominated by fiber properties [52]. Since EMAA replaced only portions of the epoxy matrix, the performance drops were minimal (<5%). However, SBS tests are more sensitive to matrix modifications [53,54] and thus an ideal geometry to examine such queries. From classical mechanics of materials, we know that the shear stress is maximum at the midplane—this is true if the material is isotropic and homogeneous. Firstly, FRCs are generally not isotropic, but often orthotropic. Secondly, more pertinent to our study, the placement of EMAA gives rise to spatial inhomogeneity. The spatial heterogeneity and the short beam length will cause the shear stress distribution along the depth to deviate from the well-known parabolic distribution, which is typically observed in long beams with homogeneous and isotropic material properties. It is, therefore, safe to conclude that placing EMAA at the mid-plane will have a considerable effect. Therefore, in addition to understanding the effect of EMAA recovery of SBS properties after healing interfacial fracture, we also study the effect of EMAA interlayers on structural integrity: both stiffness and interlaminar shear strength (ILSS).

EMAA film and mesh interlayer inclusions have shown to reduce ILSS by 33% [42] and 35% [46], respectively, while dispersed particles only produced a 22% drop [48]; though precise comparisons at constant volume fraction cannot be computed due to limited information in some of the works. Modified EMAA interlayers with additional components (i.e., carbon nanotubes (CNTs) [46]) or coatings (i.e., polyetherimide (PEI) [37]) exhibit similar declines in ILSS. Moreover, even with EMAA fibers stitched through the stacked reinforcement, thereby securing the laminate together, a drop in ILSS (similar to the mesh interlayers) of 37% is observed [43]. These reductions in virgin interlaminar shear performance are offset by large gains in mode-I fracture resistance/healing and moderate healing in repeat SBS testing [37,42,46,48]. However, limited research has been dedicated towards understanding how soft EMAA inclusions affect the overall structural response in the SBS geometry and whether such properties can be restored concurrently with mode-I fracture repair via thermal remending.

To assess the effect of thermoplastic inclusions on the SBS performance, it is crucial to fully resolve the complex stress state generated during the experiment, particularly in the subsurface regions. Since these regions are inaccessible to probing through instrumentation and imaging techniques (e.g., digital image correlation), one must resort to either analytical or numerical modeling. For long-span beams, the celebrated reduced-order mathematical model provided by Bernoulli–Euler beam theory (BEBT) offers an accurate description of the kinematics and stress state. However, for short shear beams with small span to depth ratios ≈4:1, the shear distribution deviates considerably from that of long-span beams—even under homogeneous and isotropic material properties without soft inclusions. Specifically, the shear distribution is not parabolic along the beam depth. Consequently, discrepancies arise between the BEBT-based parabolic shear stress/strain profile on the cross section (an assumption in ASTM D2344) and what is actually observed in SBS experiments; this discrepancy is more pronounced near the applied loading and support pins [55,56]. A common approach to account for this deviation is to use a shear correction factor, which is an averaging technique and may not provide sufficient granularity in the assessing the stress distribution and its extremes.

Assuming material homogeneity and isotropy, shear-corrected theories such as the Timoshenko–Ehrenfest Theory (TET) account for shear effects and deviations from the plane section hypothesis, including the non-parabolic nature of the shear stress distribution [57–59]. However, both TET and BEBT assume a homogeneous isotropic elastic constitutive law, which limits their application to anisotropic (e.g., orthotropic) composite laminates. In studies involving laminated composites — comprising multiple layers of thin laminae — more sophisticated beam and plate theories are available. For instance, third-order shear deformation theories, popularized by Reddy and co-workers [60], and layer-wise theories with variable kinematic modes [61] provide more detailed analyses. A number of studies have also sought to improve understanding of the global SBS stress and strain fields in structural fiber-composites *without* soft inclusions by leveraging numerical simulations and comparing with experiments [55,56,62–64]. For example, shear strain profiles from finite element analysis (FEA) have been validated against test data obtained from digital image correlation (DIC), showing good agreement [65,66].

However, the approaches mentioned are often inadequate for capturing the complex stress state in short beams with soft inclusions. Initially, models relied on structural theories and multi-layered elements [67], but current FRC models predominantly use homogenization-based approaches that simplify the multi-material geometries of composite microstructures [68–71]. Nonetheless, homogenized theories (e.g., shear factor correction) fail to capture stress extremes, similar to how averages may not reflect all data values. Layer-wise theories work well with flat laminates but are less effective when pockets of soft material (not in the form of lamina) are present. SBS investigations on fiber-composites with soft inclusions have been largely experimental [37,42,43,46,48], providing details of damage maps and ILSS reductions; however, the current literature offers limited insight into the underlying mechanics. Some researchers have noted that, as with plain fiber-composites (without soft inclusions), numerical modeling (e.g., FEA) is a powerful tool for assessing the mechanical intricacies of structural composites with inclusions. A few studies have investigated numerical approaches for incorporating discrete inclusions in finite element (FE) models of FRCs [72,73]. However, there is limited research utilizing FE modeling to explore SBS testing of structural composites with soft inclusions [74]. Consequently, the combined effects of the short beam stress state and more complex composite material makeups remain largely unexplored. To address this gap, we resort to three-dimensional finite element simulations, which also allow us to examine the effects of large deformations of soft material inclusions.

Another important aspect to consider is the effect of loading and supports on the stress state and the applicability of Saint-Venant's principle [75]. For long-span beams, the loading and support pins are sufficiently far from the regions of interest, allowing us to use Saint-Venant's principle to neglect their effect on the stress state in these regions [76]. However, for short shear beams, especially those made of fiber-reinforced composites (FRCs), which are orthotropic, the effect of loading and supports cannot be ignored [77–79]. Firstly, due to the size of the beam, the zone of influence — where loading and support effects are significant — might encompass the entire beam [80]. Secondly, according to the theory of anisotropic elasticity, the zone of influence related to Saint-Venant's principle enlarges under orthotropy compared to isotropic materials [81,82]. Consequently, not only does the composite matrix fall within this zone of influence, but so do the EMAA pockets. Thus, a fundamental question arises regarding modeling:

(Q4) How can we accurately account for the influence of loading and support conditions in predicting the response of short shear beams with soft inclusions?

To address the above question, we propose a novel modeling approach that breaks away from the status quo. Instead of treating loading and support pins as point loads — a common idealization — we recognize that loads and supports are distributed over a finite area. Therefore, we model these pins as rigid components and capture their interaction with the structure (i.e., the beam) using (computational) contact algorithms. This innovative approach enhances accuracy in predicting (a) the effect of EMAA pockets on structural behavior and (b) the mechanical response of EMAA pockets due to the presence of loading and supports within the zone of influence.

Having established the rationale behind this research, our approach can be summarized as follows: We combine an experimental evaluation program with finite element (FE) modeling to (a) reveal the underlying mechanisms in short beam flexure and (b) demonstrate how to mitigate structural detriment while providing capacity for self-healing. On the experimental front, we utilize a novel thermal remending platform that incorporates soft thermoplastic interlayers by 3D-printing EMAA directly onto the reinforcement fabric (Fig. 1a). The modified fiber-reinforced composite (FRC) achieves significant increases in mode-I fracture energy (G_{IC}) required to propagate a delamination (Fig. 1b)—up to 450% of that of a plain composite (Fig. 1c) [1,51]. Embedded resistive heaters enable *in situ* thermal remending below the glass transition temperature (T_g) of the thermoset epoxy matrix, and this remending is reliable up to 100+ repeated mode-I fracture/heal cycles [1]. We show that short beam shear (SBS) tests (Fig. 1d) have

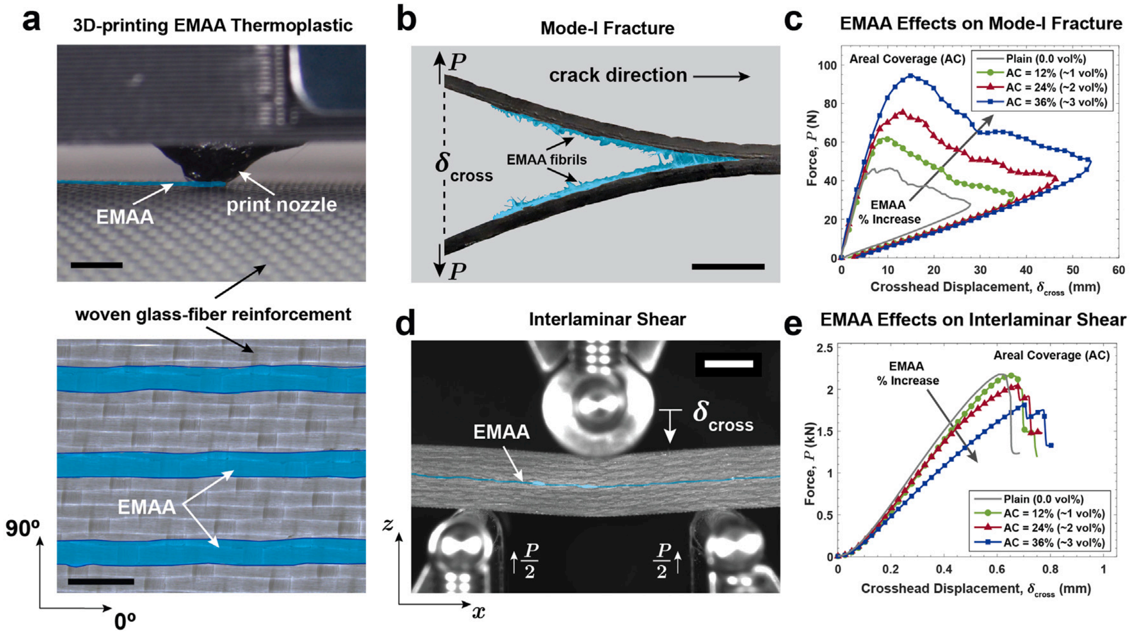

Fig. 1. Mode-I Fracture/Interlaminar Shear. (a) [top] 3D-printing of molten EMAA thermoplastic (blue color overlay) onto woven glass-fiber reinforcement (scale bar = 3 mm); [bot.] completed EMAA print aligned with textile warp (0°) direction (scale bar = 2 mm). **(b)** Mode-I fracture testing of EMAA-toughened composite (scale bar = 10 mm) and **(c)** resulting force–displacement curves for 0, 12, 24, 36% areal coverage (AC). **(d)** Short-beam-shear (SBS) 3-pt flexure testing of EMAA-toughened composite (scale bar = 3 mm) and **(e)** resulting force–displacement curves for 0–36% AC (0–3 vol%).

only minor detriments to flexural properties (Fig. 1e), indicating the effectiveness of our EMAA incorporation technique. We also undertake an extensive investigation to understand which system variables affect short-beam bending.

Using an experimentally informed computational study, we explore how the amount of EMAA and the placement of interlayers affect interlaminar shear performance. For benchmarking and ensuring the accuracy of the 3D finite element model, we first perform numerical short beam shear (SBS) simulations of “plain composites” using isotropic and orthotropic composite material models (obtained from a suite of mechanical tests) and validate these simulations against physical SBS experiments. With the validated modeling framework, we incorporate EMAA interlayers with varying individual layer areal coverages of 12, 18, 24, 30, and 36% (1–9% by volume) and vary the location and number of interlayers to study their effects on SBS stiffness and strength. Moreover, by integrating the results from the initial experiments with insights from numerical simulations, we experimentally demonstrate self-healing of both mode-I fracture and interlaminar shear over 10 fracture/repair cycles. These self-healing experiments highlight the effectiveness of our *in situ* thermal remending strategy in preserving multiple aspects of mechanical integrity, including fracture resistance and flexural strength/stiffness.

In summary, this paper addresses the fundamental questions posed above (Q1–Q4), thereby expanding the application space of self-healing in structural composites. The reported research has the potential to significantly change the landscape of repair and resilience in infrastructure, particularly for applications with extreme and evolving loading conditions.

2. Materials and methods

2.1. EMAA processing and 3D-printing

Nucrel™ 2940 EMAA (Dow Chemical, Inc.) was purchased as pellets and extruded into ≈2.5 mm diameter filament using a single screw extruder (Filastruder, Inc.) equipped with a 3 mm diameter circular die and barrel temperature of 110 °C. A rotating steel take-up cylinder (diameter = 165 mm) collected the EMAA filament while it was cooled to room temperature (RT ≈23 °C) by forced convection from a nearby fan.

EMAA filament served as the material input for fused deposition modeling (FDM) (Lulzbot, Inc.) utilizing a 500 μm diameter nozzle with a nozzle/bed temperature of 190/65 °C. EMAA was printed directly onto 8-harness (8H) satin woven E-glass reinforcement (Style 7781, Hexcel, Inc.), as depicted in Fig. 1a, ensuring strong adhesion between EMAA and glass-fibers prior to introduction of the epoxy matrix. A serpentine pattern was chosen to enable a single continuous trace with 500 ± 50 μm width and 350 ± 50 μm height, as-printed dimensions informed by prior work [51] to achieve sufficient toughening/healing. The printing orientation featured primary traces aligned parallel to the direction of the warp tows (i.e., 0° direction), illustrated in Fig. 1a.

2.2. Preform construction and composite fabrication

After printing was complete, reinforcing plies were stacked in an alternating 0°/90° orientation to complete the quasi-symmetric preform [83]. The details of each stacking sequence (including those with resistive heater interlayers) for various sample configurations are provided in their respective section.

The completed preforms underwent melt consolidation between aluminum plates (length × width × height: 405 × 405 × 6.35 mm) which were subjected to a static pressure of 1 kPa relative to the preform surface area. The full assembly was heated in a convection oven (OF-22, Cole-Parmer, Inc.) from RT to 110 °C over 15 min, where the temperature was held for 75 min, and then cooled to 60 °C over 90 min. The preform was then removed from the oven and cooled to RT by natural convection. This melt consolidation process ensures a minor increase in final composite thickness, i.e., <5% for three EMAA interlayers.

Epoxy resin (Araldite 8605, Huntsman Advanced Materials, LLC) and amine hardener (Aradur 8605, Huntsman Advanced Materials, LLC) were mixed in a 100:35 resin to hardener ratio by weight and degassed for 2 h under 12 Torr abs vacuum at RT in a drying oven (ADP 300C, Yamato, Inc.). Resin infusion via Vacuum Assisted Resin Transfer Molding (VARTM) commenced at 2 Torr (abs) until total wetting of the reinforcing preform at which point the resin inlet was clamped shut and the vacuum was decreased to 380 Torr (abs) and held for 24 h at RT to achieve matrix solidification. A final cure followed for 2 h at 121 °C and 2 h at 150 °C to yield a composite glass-transition temperature of ≈145 °C, as measured by dynamic mechanical analysis (DMA) according to ASTM E1640.

2.3. Mode-I fracture

2.3.1. Double cantilever beam (DCB) sample fabrication

Plain glass fiber-reinforced polymer (GFRP) composite fracture samples (≈4 mm thick) were composed of sixteen E-glass plies and two proprietary non-woven resistive heater interlayers (≈100 μm thick with randomly oriented carbon and glass fibers) placed between the 5/6th and 11/12th layers for a stacking sequence of $[90/0]_2$/90-heater-$[0/90]_3$-heater-0/$[90/0]_2$. For self-healing composites, EMAA interlayers were incorporated at the midplane at 36% areal coverage leading to a final stacking sequence of $[90/0]_2$/90-heater-[0/90/0]-EMAA-[90/0/90]-heater-0/$[90/0]_2$. Prior to incorporation into the layup, a 10 mm conductive silver coating was applied to the top and bottom edges of the heaters and dried for 30 min before adhering a 10 mm section of conductive copper tape (bus bar) for external electrical connections. A 25 μm thick ethylene tetrafluoroethylene (ETFE) film (50 mm long) was placed at the midplane to serve as a pre-crack for fracture experiments. The preform then underwent melt consolidation, VARTM, and curing as described above.

Samples were sectioned to 25 mm wide by 150 mm long using a diamond-blade wet saw (41-AR, Sowers Dia-Met, Inc.), exposing the resistive heater bus bars. A 0.65 mm diameter center hole was drilled 4 mm deep into each of the four exposed bus bars and a copper wire (0.64 mm diameter) was inserted into each hole. These external electrical connections were potted with a 5 min epoxy and allowed to sit for 24 h at RT. The top face of each fracture sample was painted matte black for infrared (IR) imaging during healing via thermal remending. Steel hinges were bonded to the top/bottom composite faces on the pre-crack sample-end with a structural adhesive (DP460NS, 3M, Inc.) and cured at RT for 24 h followed by an additional 4 h at 49 °C. A straight line was marked on the bottom of the sample 50 mm from the interior edge of the ETFE film to designate the prescribed crack propagation length.

2.3.2. Mode-I fracture testing

DCB samples were tested in mode-I fracture according to ASTM D5528 on a 5 kN electromechanical load frame (Alliance RT/5, MTS, Inc.) equipped with a 250 N load cell. Displacement-controlled loading at a rate of 5 mm/min propagated a delamination from the pre-crack interior edge along the midplane of the sample. A 4K resolution webcam (Logitech BRIO), equipped with a custom macro lens (LM12JC5M2, Kowa Optical Products Co., Ltd.) monitored crack growth from the bottom surface of the translucent glass-fiber composites, assisted via a backlight (MI-150, Dolan-Jenner, Inc.) to enhance contrast between the crack front and undamaged region. The samples exhibited linear elastic behavior until crack initiation, after which the load steadily drops as the crack propagates to an incremental length of Δa = 50 mm. The sample was then unloaded to zero crosshead displacement.

2.3.3. Fracture energy quantification

Fracture resistance was quantified via mode-I critical strain energy release rate (G_{IC}), which measures the energy required to propagate the crack normalized by the area of the fractured interface. The area method was used to calculate a single G_{IC} value for each 50 mm fracture event. Under this method, the formula for G_{IC} takes the following form:

$$G_{IC} = \frac{1}{b}\frac{\Delta U}{\Delta a}, \tag{1}$$

where b denotes the sample width, Δa is the linear distance of crack propagation, and ΔU represents the energy required to create the new crack surfaces defined by the area enclosed within the force–displacement curve [1,28,29,84]. For an applied crosshead displacement δ_{cross}, the energy increment ΔU can be written as follows:

$$\Delta U = \int_0^{\delta_{cross}} P\, d\delta_{cross}\Big|_{\Delta a}, \tag{2}$$

where P is the resulting force.

2.3.4. In situ thermal remending

After unloading, *in situ* self-healing via thermal remending was performed in the load frame at zero crosshead displacement. A DC power supply (PWS4602, Tektronix, Inc.) provided electrical power (≈15 W) to the embedded resistive heaters to reach a target maximum top surface healing temperature of 130 °C as monitored by an overhead IR camera (A600, Teledyne FLIR, Inc.). Power was applied for a total of 15 min before disconnecting and convectively cooling for 30 min to RT. A total of 10 fracture/heal cycles were performed for each sample tested.

To quantify efficacy, we used healing efficiency ($\hat{\eta}$), defined as the ratio between healed and virgin critical strain energy release rates, and expressed as a percentage [1,28,29]. Mathematically,

$$\hat{\eta} = \frac{G_{IC}^{healed}}{G_{IC}^{virgin}} \times 100\%, \tag{3}$$

where G_{IC}^{virgin} and G_{IC}^{healed} represent the virgin and healed critical strain energy release rates, respectively.

2.4. 3-pt flexure

2.4.1. Short beam shear (SBS) sample fabrication

Plain SBS shear samples (≈4 mm thick) comprised sixteen E-glass plies with a stacking sequence of $[90/0]_8$. Stacking sequences for samples augmented with EMAA are described later as motivated by numerical simulations. Preforms containing EMAA underwent the same melt consolidation, VARTM, and curing steps as the DCB fracture samples, after which these were sectioned and polished to 8.3 mm wide by 38 mm long using a diamond-blade wet saw (41-AR, Sowers Dia-Met, Inc.) and rotary polisher (Allied High Tech Products, Inc.).

To evaluate the interlaminar shear performance of fractured/healed composites, SBS samples of the same dimensions (8.3 × 38 × 4 mm) were excised from the undamaged, fractured, and healed regions of the DCBs. This was performed after a specified number of DCB fracture/heal cycles (i.e., virgin fracture, virgin fracture + 1 heal cycle, virgin + 5 heal cycles, and virgin + 10 heal cycles).

2.4.2. 3-pt flexure testing

SBS samples were tested in 3-pt flexure according to ASTM D2344 on a 100 kN electromechanical load frame (Exceed E45, MTS, Inc.). A span:depth ratio of 4:1 was employed with loading/support pins of diameter 6.35/3.175 mm, respectively (Fig. 2a). Displacement-controlled loading at a rate of 1.5 mm/min continued until failure occurred—as defined by an ≈25% drop in the highest load. Digital image correlation (DIC) was utilized via a 12.3 MP camera (GS3-U3-123S6M-C, Teledyne FLIR, Inc.) on the front sample surface, which was painted matte white and speckled black as shown in Fig. 2b. Correlated images were post-processed with Vic-2D software (Version 2009.1.0, Correlated Solutions, Inc.) to measure the applied midspan displacement by subtracting the displacement directly above the support pins from the displacement directly below the loading pin ($\delta_{calc} = \delta_{top}^{DIC} - \delta_{bot}^{DIC}$). As shown in Fig. 2c, this applied displacement is markedly different than the recorded crosshead value (δ_{cross}), and thus, should be calculated to accurately represent the true displacement of the beam. In addition to the applied vertical displacement, DIC also provides the full field displacement/strain profiles at different stages of the applied loading.

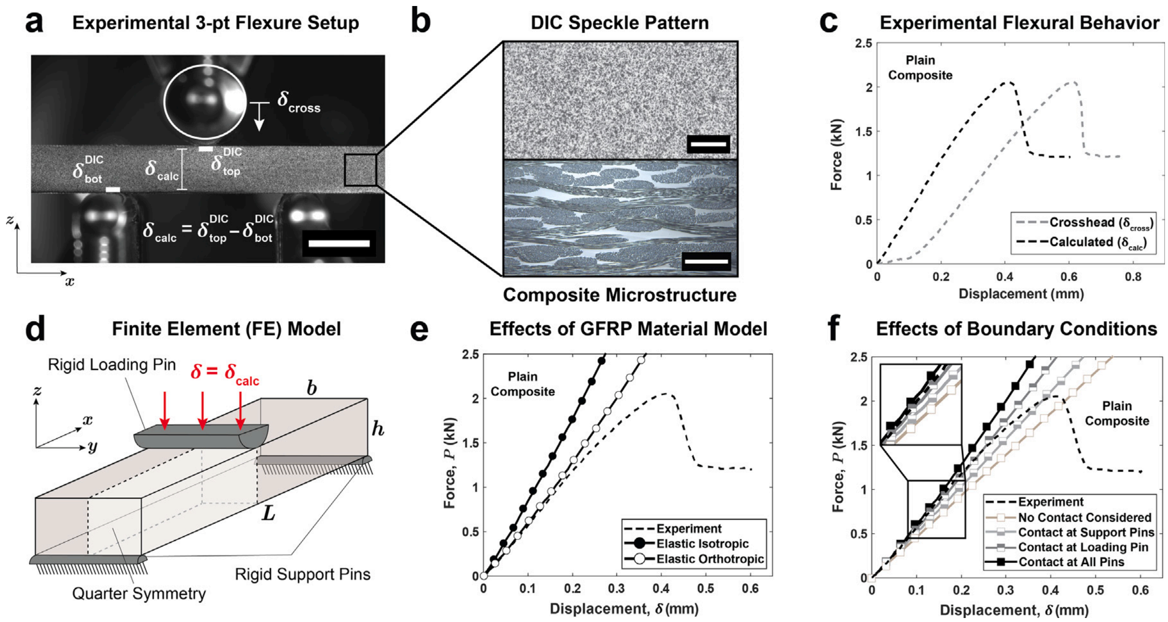

Fig. 2. Experimental/Numerical Setup. (a) Experimental 3-pt flexure test setup defining crosshead and DIC displacement measures (scale bar = 5 mm). **(b)** [top] DIC speckle pattern (scale bar = 500 μm); [bot.] woven composite microstructure (scale bar = 250 μm). **(c)** Experimental force–displacement curve comparison of the crosshead (δ_{cross}) and the calculated DIC displacement (δ_{calc}) for a plain composite. **(d)** Numerical (i.e., finite element) model setup with fixed rigid support pins and displacement applied ($\delta = \delta_{\mathrm{calc}}$) to the rigid loading pin. **(e)** Comparison of numerical force–displacement curves for linear elastic isotropic and linear elastic orthotropic composite material models versus the experimental curve (δ_{calc}). **(f)** Comparison of the experimental force–displacement behavior versus numerical responses for different contact conditions at the loading/support pins.

2.4.3. Interlaminar shear property quantification

Two metrics were used to quantify interlaminar shear behavior: stiffness and strength. Stiffness was obtained via a linear regression of the force–displacement curves (δ_{calc} = 0.05 to 0.25 mm). Interlaminar shear strength (ILSS) calculated according to ASTM D2344, is the maximum shear force ($P/2$) divided by the area ($A = bh$) of the rectangular cross-section and multiplied by a factor of 3/2 as derived from BEBT (i.e., considering the first and second moment of areas about the neutral axis):

$$ILSS = \frac{3P}{4bh}, \tag{4}$$

where b and h are the beam width and height/thickness, respectively.

2.5. Visualization

We employed optical microscopy to visualize EMAA/fiber-composite geometries and investigate the interlaminar shear damage modes. Images were acquired with a digital light microscope (AXIO Zoom V.16, Zeiss, Inc.) equipped with an LED ring light and coaxial polarizer. For imaging shear damage, a fluorescent dye penetrant comprised of a mixture of Coumarin 480 (Exciton, Inc.) in ethanol (100:38 by weight) was infiltrated into surface cracks and excited via a metal-halide lamp (centered at 350 ± 25 nm) with a longpass optical filter (>425 nm).

2.6. Numerical simulations

2.6.1. Finite element model setup

To assess the mechanical response of FRC with soft thermoplastic inclusions, we developed finite element (FE) models of the SBS test in Abaqus (CAE 2022, ABAQUS Inc.). We considered a simply supported beam with a 4:1 span-to-depth ratio and applied a midspan displacement on the beam's top surface through a rigid loading pin (diameter = 6.35 mm). The sample was supported by two smaller pins (diameter = 3.175 mm) on the bottom surface, mimicking the experimental setup. We exploited symmetry across the xz- and yz-planes (Fig. 2d) to build a quarter symmetric model [85], and reduce computational cost. The beam was discretized using standard quadratic hexahedral elements (C3D20) to avoid shear locking and hourglass mode, with a maximum size of 0.07 mm in cross-section (yz-plane) and maximum aspect ratio of 3:1 along the beam length (x-axis). The mesh configuration ensured a converged numerical solution (see Section S1), and the EMAA domains included at least two layers of elements along the shortest dimension. Note that all of the simulations in this study assume perfect bonding between interfaces, which is enforced using geometric compatibility constraints. We first modeled a plain composite and investigated different assumptions (i.e., material/geometric linearity, boundary conditions) to attain model accuracy while maintaining computational efficiency.

2.6.2. Material properties

Due to the anisotropic (i.e., orthotropic) nature of the composite, we performed a suite of mechanical tests to obtain material properties in different directions according to their respective ASTM standards: in-plane tension (ASTM D3039), through-thickness tension (ASTM D7291), and in-plane/through-thickness Iosipescu shear (ASTM D5379). We initially compared two approaches for the composite material model: a homogenized *isotropic* elastic material based on the in-plane properties (E_x, υ_{xy}), and a homogenized *orthotropic* elastic model informed by elastic properties from both in-plane and through-thickness mechanical tests (E_x, υ_{xy}, G_{xy}, E_z, υ_{xz}, G_{xz}). While the material is inherently orthotropic, an isotropic model is appealing due to its simplicity given the difficulty in obtaining detailed orthotropic properties (described in detail in Section S2). Simulation results, however, showed that the homogenized isotropy approximation leads to significant deviation from observed experimental behavior even in the elastic regime, as shown in Fig. 2e. Alternatively, implementing an orthotropic material model resulted in better agreement with experimental data. These observations underscore the importance of explicitly modeling the lower through-thickness modulus. Thus, all subsequent numerical investigations in this study are based on the orthotropic constitutive model informed by experimental test data.

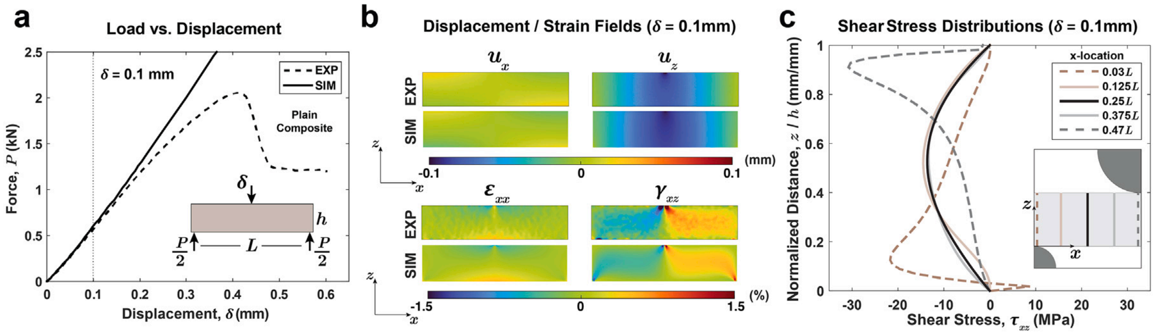

Fig. 3. Model Validation for Plain Composite. (a) Plain GFRP force–displacement ($\delta = \delta_{calc}$) curve comparison between experiments (EXP) and simulations (SIM) with a linear orthotropic GFRP material model and contact enforced at all loading/support pins. **(b)** Comparison between experimental and numerical displacement and strain contours at 0.1 mm applied displacement. **(c)** Numerical shear stress cross-sectional profiles at different points along the beam (for 0.1 mm applied displacement) indicating local shear stress maxima at the midplane and outer surfaces.

2.6.3. Loading and boundary conditions

We first modeled the SBS load and support mechanisms using standard Dirichlet boundary conditions. For the simply supported beam considered in this study, we restrained both bottom edges of the beam against vertical motion, while also restraining one edge horizontally to prevent rigid-body motion. Load was then applied by prescribing vertical displacements along the top surface at midspan. These assumptions produce a linear force vs. displacement response under elasticity conditions, therefore simplifying the simulation process. Numerical results in Fig. 2f, however, revealed that this approach (considering no contact) produces inaccurate results. Close inspection shows that the line-based Dirichlet boundary conditions act as concentrated forces, causing high stress concentrations at the loading and support pin locations and leading to a more compliant response. This effect was not consistent with the test conditions, where loads and reactions are supplied through a finite area of contact with cylindrical pins. Therefore, to better approximate the experimental setup, we incorporated non-deformable (i.e., rigid) pins at load and support locations and explicitly model the contact mechanisms. We assumed frictionless contact with rigid, no-penetration constraints enforced against an analytical cylindrical pin geometry implemented via the surface-to-surface algorithm in Abaqus. Although enforcing contact constraints requires a nonlinear solver with a longer run time, Fig. 2f shows modeling contact at both loading and support pins is required to best accurately represent the experimental results. To identify which contact event (at the loading or support pins) has a greater effect on accuracy, we repeated the analysis with contact constraints enforced at the load and support pins independently, and find that contact at the support pins plays a more significant role in the overall response. This is due to the fact that, even though the support pins are smaller in diameter, the contact area at the support is larger than the contact area at the loading pin due to the sliding of the sample over the support pin, which produces lower stress concentrations. This is a noteworthy finding given that ASTM D2344 emphasizes stress concentration at the loading pin, but does not mention the effects at the supports. As discussed later, accurately modeling the support boundary conditions becomes even more critical when incorporating EMAA interlayers.

It is important to note that, in all numerical studies, the beam length was only modeled up to the support centerlines. Numerical simulations using the full length beam, including the unloaded regions beyond the supports showed no difference in behavior.

2.6.4. Experimental validation

After determining the experimental and numerical considerations to accurately capture the flexural load vs. midspan displacement response for plain composites (Fig. 3a), we further validated the numerical model by comparing the full field displacement and strain profiles with those measured via DIC (Fig. 3b). Results showed excellent agreement between numerical results and experimental measurements. The negative vertical displacement of the beam (u_z) caused the region above the neutral axis to be in compression and the region below to be in tension as depicted by the axial displacements/strains (u_x/ε_x), but the magnitudes of each remain fairly low. Moreover, high shear strains (γ_{xz}) were observed emanating from the loading/support pins to reach a local maximum at the neutral axis midway between the pins.

We leveraged the detailed stress data provided by the computational model to study the distribution of shear stresses (τ_{xz}) along the sample cross-section. We plotted the shear stresses along the cross-section at increasing distances from the left support, as depicted in Fig. 3c. Results showed that there are three distinct regions of interest. In the vicinity of the loading/support pins ($<L/30$), the maximum shear stress occurs near the top/bottom surfaces, respectively. In between the loading/support pins ($L/4$) the maximum shear stress occurred at the neutral axis of the sample. These observations confirmed that the parabolic shear distribution assumption (*viz* BEBT and underlying ASTM D2344) is only valid at undisturbed locations away from the load/support pins ($>L/30$). Based on these results, a subsequent study was conducted to investigate the structural effects of soft EMAA interlayers located at each of these three critical (high stress/strain) locations (i.e., laminate midplane and near the top/bottom surfaces).

2.6.5. EMAA incorporation

Based on the three critical z-locations identified by FE simulations, we defined three sample types: (i) samples with EMAA only at the midplane (M) comprising: $[90/0]_4$-EMAA-$[90/0]_4$, (ii) samples with EMAA near the outer surfaces (O) between layers 2/3 and 14/15 designated: [90/0]-EMAA-$[90/0]_6$-EMAA-[90/0], and (iii) samples with EMAA at the midplane and near the outer surfaces (M+O) denoted: [90/0]-EMAA-$[90/0]_3$-EMAA-$[90/0]_3$-EMAA-[90/0]. For each of the mid (M), outer (O), and mid-plus-outer (M+O) sample types, the areal coverage of each EMAA layer was varied between 12, 18, 24, 30, and 36% with global vol.% ranging from 1.0 to 8.6%. Representative cross-sections from the experiments and numerical model are shown in Fig. 4a for 24% areal coverage per layer. The irregular, nested EMAA cross-sections from physical samples were approximated as rectangular domains 1.2 mm wide × 0.14 mm thick (taken from averaged measurements of experimental domains) as shown in the inset of Fig. 4b. The numerical model employed a conforming mesh at the EMAA-composite interface to ensure accuracy of the stress field and assumes that the soft thermoplastic inclusions remain bonded to the composite throughout the analysis. The model was also built such that each distinct domain (e.g., the EMAA inclusions) contain at least two elements across its shortest dimension. We performed uniaxial tension tests on EMAA polymer dogbone samples in accordance with ASTM D638 to experimentally characterize EMAA (see Section S3), and investigate two material models for the isotropic EMAA inclusions: a

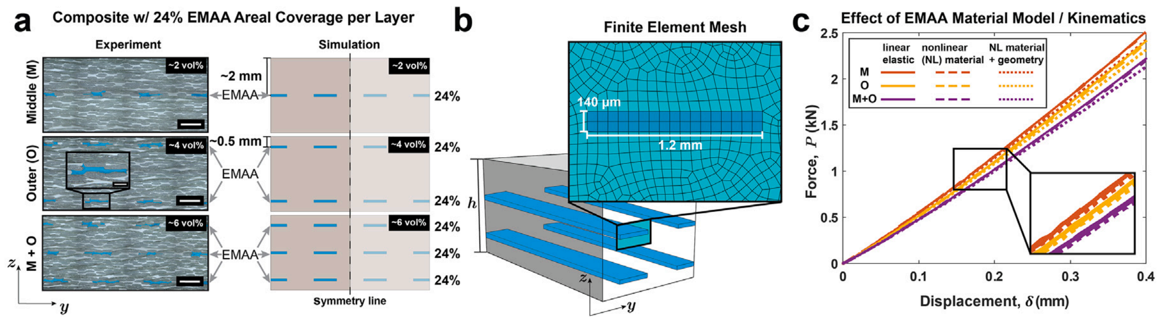

Fig. 4. EMAA Augmented Composite Setup. (a) Experimental/numerical cross-sectional geometries for middle (M), outer (O), and middle + outer (M+O) sample types at 24% areal coverage (AC) per layer (main scale bars = 1 mm, inset scale bar = 250 μm). **(b)** Finite element mesh of EMAA domains and surrounding composite. **(c)** Comparison of numerical force–displacement curves for M, O, and M+O sample types at 24% AC per layer with linear elastic EMAA material model and linearized strains, nonlinear (NL) EMAA material and linearized strains, and NL EMAA material plus NL geometry (i.e., finite deformation).

linear elastic model and a nonlinear model that incorporates the full stress vs. strain data obtained from such experiments. Since the soft inclusions were expected to undergo large strains, we also assessed the impact of large (i.e., finite) deformation kinematics on sample response. Fig. 4c shows that for all sample types (M, O, M+O) neither nonlinear EMAA material behavior nor finite deformation kinematics produced a significant change in the force–displacement response. Therefore, we selected a linear EMAA material model considering small deformations/strains for computational efficiency.

3. Results and discussion

3.1. EMAA effects on short beam shear

Fig. 5a shows the effect of EMAA incorporated in each of the three sample types (M, O, M+O) by comparing force versus displacement behavior between experiments and simulations with 24% areal coverage (AC) per layer (i.e.,vol% of 1.9, 3.8, and 5.7, respectively). Note that the force–displacement curves for all EMAA areal coverages studied (12, 18, 24, 30, 36%) are shown in Section S4. Fig. 5b quantifies the flexural stiffness (k) effect for experiments by taking a linear regression between 0.05 and 0.25 mm of the displacement (δ). Below 24% AC of EMAA per layer results in ≥85% retention of the experimentally measured plain composite stiffness. Above 24% AC, the stiffness of samples with an EMAA midlayer (i.e., M and M+O) declines more rapidly than O-type samples. For example, at 36% AC per layer, M and M+O type samples retain ≈65% stiffness while O-type samples retain ≈88%, which is especially interesting when one considers that O-type samples have twice the volume percent (5.7%) of EMAA compared to M-type samples (2.9%). This indicates that the EMAA interlayer location has a more dominant effect on SBS stiffness than the global volume percentage, a new finding from this study.

The numerical model though, predicts that M-type samples should be stiffer than O-type samples as shown in Fig. 5c. The discrepancy in stiffness trends for M- and O-type samples between experiments and simulations can be explained by examination of the strain profiles in Fig. 5d. The highest shear strains are largely incurred along the sample midplane especially when an EMAA midlayer is included. These high midplane shear strains cause damage to the composite sections between EMAA traces at the midplane [48]. The damaged regions decrease the global stiffness of the composite by degrading the load transfer from one reinforcing ply to the next. This is seen in the physical experiments, but not captured in the simulations that assume elastic materials. The experimental/numerical discrepancy is not observed at lower areal coverages (<24%) because the midplane strains remain low enough (≈0.4%) to not cause significant damage in FRC domains.

Strength retention also follows a slowly decreasing trend with increasing areal coverage (Fig. 5e), where at 24% AC per layer, 92% of the plain composite ILSS is retained in each sample type. It is important to emphasize that the relatively minor decrease in strength/stiffness (8%/15%) observed at this intermediate 24% AC, which in prior works produced nearly 300% toughening and healing efficiencies approaching 100% for 100+ mode-I fracture cycles [1,51], indicates a reasonable trade-off for high toughening/healing and minimal detriments in SBS. Even at the maximum areal coverage of 36% per layer, each of the M, O, and M+O sample types outperform prior studies [37,42,43,46,48] with a strength retention of ≈83%, regardless of EMAA location. The independence of EMAA placement on ILSS differs from the results for stiffness, which show that EMAA located at the midplane (rather than the outer layers) causes greater detriment to stiffness at higher areal coverage. EMAA interlayer location also influences the failure mode as shown in Fig. 5f. For plain composites, distributed interlaminar shear cracking occurs throughout the sample cross-section extending from the loading pin to the support pin along a 45° line. With a single EMAA midlayer, the failure mode transitions to tensile fiber rupture at the bottom surface, which is an undesirable damage mode that is currently unhealable by our EMAA thermal remending strategy. However, when outer interlayers are included (i.e., for O and M+O samples), the healable delamination failure mode is again recovered. This newfound understanding for tailored EMAA placement demonstrates the ability to steer the failure mode towards healable interlaminar damage.

3.2. Self-healing mode-I fracture and short beam shear property recovery

Due to composite internal damage (e.g., fiber-rupture) and resulting permanent deformation of an SBS sample after failure (i.e., no longer a straight beam), it is difficult to accurately evaluate the ILSS in repeat 3-pt flexure tests. Therefore, we first conduct mode-I fracture/healing experiments on double cantilever beam (DCB) specimens (that produce only elastic strains in the composite beams) for: virgin (one fracture/no healing), virgin + 1 heal cycle, virgin + 5 heal cycles, and virgin + 10 heal cycles. Then SBS samples are excised from both: (i) a region that is fractured/healed, and (ii) from an undamaged region that was not fractured, but was heated/cooled with each *in situ* self-healing cycle (i.e., scientific control). To the best of our knowledge, this is the first time the measured stiffness and strength (i.e., ILSS) of SBS samples (without internal damage) can be accurately compared to virgin states. EMAA-augmented samples are also compared to plain composite controls (i.e., without healing agent) in their undamaged and fractured states. For all samples containing healing agent, EMAA is incorporated at the midplane at the maximum 36% areal coverage to determine any self-healing benefits for a sample configuration with the greatest detriment to SBS stiffness and strength (as discussed prior).

Fig. 6a depicts the mode-I fracture force–displacement curves for the virgin and 1, 5, and 10 heal cycles showing a progressive increase in recovery and eventual convergence to the original virgin state by heal

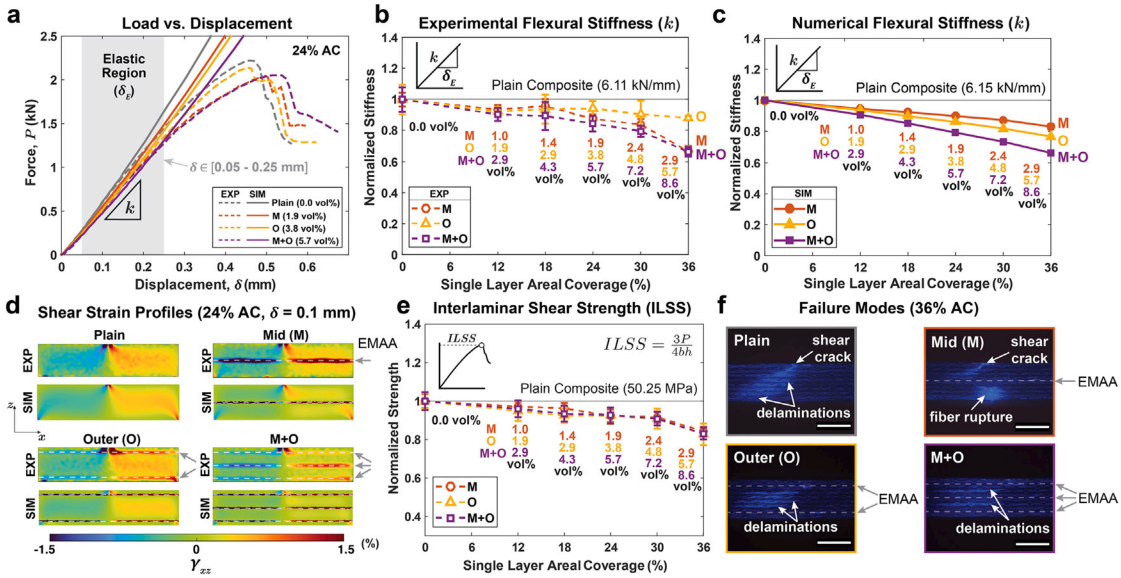

Fig. 5. Effect of EMAA Interlayers on Interlaminar Shear. (a) Comparison of experimental/numerical force–displacement curves for M, O, and M+O sample types at 24% areal coverage (AC) per layer. **(b)** Experimental stiffness measurements for M, O, and M+O samples for AC varying between 0 and 36% per layer. Error bars indicate the standard deviation from the mean ($n \geq 3$). **(c)** Numerical stiffness measurements for M, O, and M+O samples with AC varying between 0 and 36% per layer. **(d)** Experimental/numerical shear strain profile comparison at 0.1 mm applied displacement. **(e)** Experimental interlaminar shear strength (ILSS) for M, O, and M+O sample types with AC varying between 0 and 36% per layer. Error bars indicate the standard deviation from the mean (n = 6). **(f)** Failure mode comparison for M, O, and M+O sample types at 36% AC versus a plain composite control (scale bars = 5 mm).

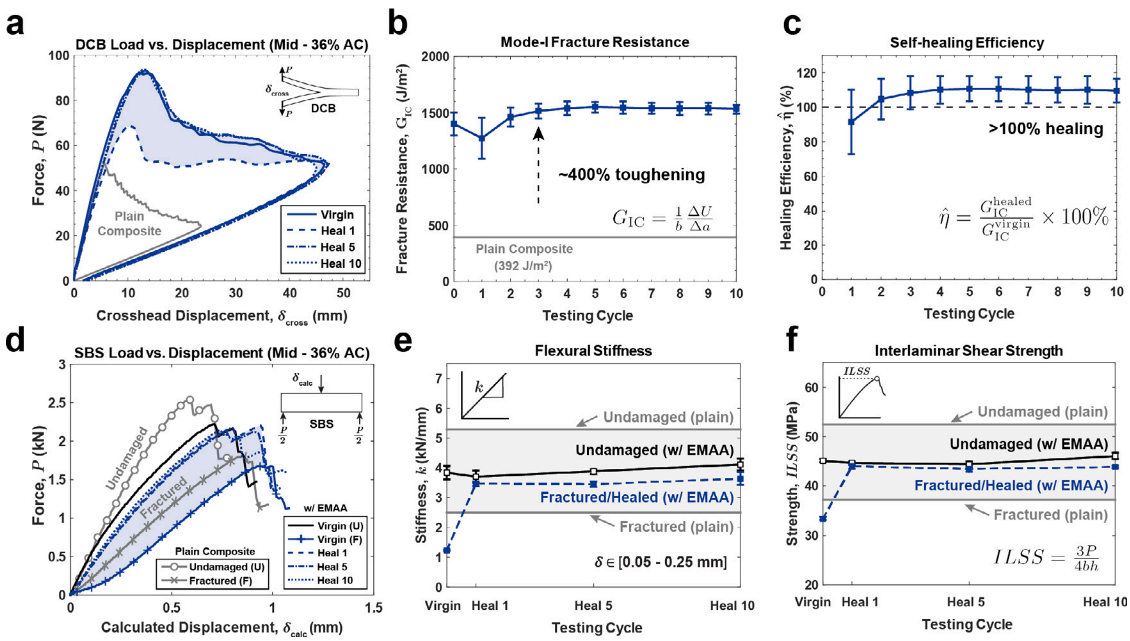

Fig. 6. Self-healing Double Cantilever Beam (DCB) and Short Beam Shear (SBS) Property Recovery. (a) Representative DCB mode-I fracture force–displacement curves (virgin and up to 10 heal cycles) for 36% EMAA midplane areal coverage (AC) alongside a non-healing plain composite control. **(b)** Fracture resistance, (i.e., critical strain energy release rate, G_{IC}) for all test cycles. **(c)** Self-healing efficiency ($\hat{\eta}$) for 10 heal cycles. Error bars in (b) and (c) indicate the standard deviation from the mean (n = 3). **(d)** Representative SBS 3-pt flexure force–displacement curves for undamaged and fractured/healed specimens (36% EMAA midplane AC) alongside a plain composite control. **(e)** Flexural stiffness (k) evolution. **(f)** Interlaminar shear strength ($ILSS$) evolution. Error bars in (e) and (f) indicate the standard deviation from the mean (n = 4).

cycle 5. Mode-I strain energy release rate (G_{IC}) and healing efficiency ($\hat{\eta}$) are shown in Fig. 6b and 6c respectively, where ≈400% toughening is achieved compared to a plain composite (G_{IC} = 392 J/m^2) and healing efficiency exceeds 100% of the toughened value over the 10 heal cycles. These favorable attributes (e.g., full fracture recovery) over repeated heal cycles are, in part, due to low melt-viscosity of EMAA [47] and the well-documented chemical/physical pressure delivery mechanism [1,36] that helps spread the molten healing agent within the damage zone and re-bond a greater portion of the fractured interfaces. Cross-sectional images of a composite laminate containing EMAA before fracture, post-fracture, and after self-healing are shown in Section S5.

From 3-pt flexure testing of SBS samples excised from DCBs, the undamaged and fractured plain composite force–displacement curves respectively define the upper and lower bounds for non-healed counterparts as shown in Fig. 6d. The SBS stiffness and strength values are quantified in Fig. 6e and 6f, respectively. Similar to prior SBS results (i.e., Fig. 5b), the flexural stiffness/strength of an *undamaged* EMAA-modified composite falls below that of an undamaged plain composite, indicating a reduction in structural capacity. Moreover, a *fractured* composite containing EMAA (prior to healing) also falls below the flexural performance of a fractured plain composite due to the combined detriment of the soft inclusions and full-length midplane fracture. However, after just one heal cycle, nearly full recovery in SBS stiffness/strength (i.e., 94/98%) is attained whereby the mechanical behavior of the healed composite approaches its undamaged state. Structural property restoration is maintained after repeated fracture/heal cycles, up to ten in this study, but presumably capable of an order of magnitude more based on prior trends with the same thermal remending approach [1]. In short, this latest demonstration reveals a self-healing structural FRC that is able to achieve repeated and simultaneous recovery of both mode-I fracture resistance and short beam flexural stiffness/strength.

4. Conclusions

This article presents (i) experimental considerations required to accurately characterize the constitutive properties of anisotropic fiber-reinforced composites containing an isotropic thermoplastic healing agent, (ii) numerical modeling aspects related to material/geometric properties and boundary conditions, (iii) combined mechanistic insight into how soft thermoplastic interlayer inclusions can impact structural performance, and (iv) a demonstration of repeated self-healing of both mode-I fracture (i.e., double cantilever beam, DCB) and 3-pt flexure (i.e., short-beam shear, SBS) properties.

To obtain good agreement between SBS experiments and simulations (i.e., validation), herein in the elastic regime, it is necessary to perform a suite of constituent-level tests with full-field displacement/strain profiles to capture the orthotropic composite response and model appropriate loading/boundary conditions including contact at both the loading pin and supports. Once validation is obtained for plain composite laminates, 3D-printed thermoplastic interlayers are incorporated in the most critical stress regions (i.e., at the midplane and near outer surfaces) to probe the maximum effect on SBS elastic and failure performance. The largest reduction in stiffness occurs when EMAA is only included at the midlayer where pronounced shear strains (due to the compliant EMAA) lead to damage in the adjacent composite. EMAA placed near the two outer surfaces only exhibit relatively minor stiffness effects with a 88% retention even at the maximum 36% areal coverage (AC) per layer. Interestingly, the impact of EMAA inclusions on ILSS, unlike stiffness, is independent of interlayer location and is instead governed by the areal coverage in each layer with 92% retention at 24% AC and 83% retention at 36% AC. While statistically EMAA location does not effect the magnitude of ILSS, it does dictate the damage mode and can therefore be leveraged to mitigate fiber rupture and instead obtain healable interlaminar shear cracking. Finally, the ability to heal nearly 100% of both mode-I fracture resistance and interlaminar shear stiffness/strength is demonstrated over 10 consecutive mechanical load cycles, affirming a multi-functional composite that can resist and restore structural damage under multiple loading scenarios (i.e., stress states).

A promising direction for future research is to develop a microstructure-informed damage and fracture modeling framework that can capture the behavior of self-healed materials up to failure, extending beyond the elastic regime. Once this predictive framework is established, it will be possible to utilize machine learning (ML) algorithms to create fast-forecasting models suitable for more efficient and larger-scale analyses.

CRediT authorship contribution statement

Jack S. Turicek: Writing – review & editing, Writing – original draft, Visualization, Investigation, Formal analysis. **Vikita Kamala:** Writing – review & editing, Writing – original draft, Visualization, Investigation, Formal analysis. **Kalyana B. Nakshatrala:** Writing – review & editing, Writing – original draft. **Ghadir Haikal:** Writing – review & editing, Writing – original draft, Supervision, Project administration, Methodology, Data curation. **Jason F. Patrick:** Writing – review & editing, Writing – original draft, Supervision, Project administration, Methodology, Funding acquisition, Data curation, Conceptualization.

Declaration of competing interest

The authors declare the following financial interests/personal relationships which may be considered as potential competing interests: Jason Patrick reports financial support was provided by Strategic Environmental Research and Development Program. Jason Patrick is an inventor on a patent #US 11,613,088 B2 issued to NC State University. If there are other authors, they declare that they have no known competing financial interests or personal relationships that could have appeared to influence the work reported in this paper.

Acknowledgments

The authors acknowledge the financial support from the Strategic Environmental Research and Development Program (SERDP) through grant No. W912HQ21C0044 awarded to J.F.P. and funding provided to G.H. by NC State University. The work was performed in part at the Analytical Instrumentation Facility (AIF) at NC State University, which is supported by the State of North Carolina and the National Science Foundation (grant ECCS-2025064). This material is based upon work supported by the National Science Foundation Graduate Research Fellowship Program under Grant No. DGE-2137100. Any opinions, findings, and conclusions or recommendations expressed in this material are those of the author(s) and do not necessarily reflect the views of the National Science Foundation.

Appendix A. Supplementary data

Supplementary material related to this article can be found online at https://doi.org/10.1016/j.compositesa.2025.108803.

Data availability

Data will be made available on request.

References

[1] Snyder AD, Phillips ZJ, Turicek JS, Diesendruck CE, Nakshatrala KB, Patrick JF. Prolonged in situ self-healing in structural composites via thermo-reversible entanglement. Nat Commun 2022;13(1):1–12.

[2] Measures RM. Smart composite structures with embedded sensors. Compos Eng 1992;2:597–618.

[3] Toohey KS, Sottos NR, Lewis JA, Moore JS, White SR. Self-healing materials with microvascular networks. Nat Mater 2007;6:581–5.

[4] Wisnom MR. The role of delamination in failure of fibre-reinforced composites. Philos Trans R Soc A: Math Phys Eng Sci 2012;370(1965):1850–70.

[5] Ye L. Evaluation of mode-I interlaminar fracture toughness for fiber-reinforced composite materials. Compos Sci Technol 1992;43(1):49–54.

[6] McKenna GB. Interlaminar effects in fiber-reinforced plastics - A review. Polym-Plast Technol Eng 1975;5(1):23–53.

[7] Katnam KB, Da Silva LFM, Young TM. Bonded repair of composite aircraft structures: A review of scientific challenges and opportunities. Prog Aerosp Sci 2013;61:26–42.

[8] Heslehurst RB. Engineered repairs of composite structures. first ed. Boca Raton: CRC Press / Taylor & Francis; 2019.

[9] Kinloch A, Shaw S, Tod D, Hunston D. Deformation and fracture behaviour of a rubber-toughened epoxy: 1. Microstructure and fracture studies. Polymer 1983;24(10):1341–54.
[10] Nair SV, Subramaniam A, Goettler LA. Fracture resistance of polyblends and polyblend matrix composites: Part II Role of the rubber phase in Nylon 6,6/ABS alloys. J Mater Sci 1997;32:5347–54.
[11] Hodgkin JH, Simon GP, Varley RJ. Thermoplastic toughening of epoxy resins: a critical review. Polym Adv Technol 1998;9(1):3–10.
[12] Awang Ngah S, Taylor AC. Toughening performance of glass fibre composites with core–shell rubber and silica nanoparticle modified matrices. Compos Part A: Appl Sci Manuf 2016;80:292–303.
[13] Matsuda S, Hojo M, Ochiai S, Murakami A, Akimoto H, Ando M. Effect of ionomer thickness on mode I interlaminar fracture toughness for ionomer toughened CFRP. Compos Part A: Appl Sci Manuf 1999;30:1311–9.
[14] Sela N, Ishai O, Banks-Sills L. The effect of adhesive thickness on interlaminar fracture toughness of interleaved CFRP specimens. Composites 1989;20:257–64.
[15] Vallack N, Sampson WW. Materials systems for interleave toughening in polymer composites. J Mater Sci 2022;57:6129–56.
[16] Blaiszik BJ, Kramer SLB, Olugebefola SC, Moore JS, Sottos NR, White SR. Self-healing polymers and composites. Annu Rev Mater Res 2010;40(1):179–211.
[17] Cohades A, Branfoot C, Rae S, Bond I, Michaud V. Progress in self-healing fiber-reinforced polymer composites. Adv Mater Interfaces 2018;5(17):1–20.
[18] Diesendruck CE, Sottos NR, Moore JS, White SR. Biomimetic self-healing. Angew Chem Int Ed 2015;54(36):10428–47.
[19] Patrick JF, Robb MJ, Sottos NR, Moore JS, White SR. Polymers with autonomous life-cycle control. Nature 2016;540(7633):363–70.
[20] Bekas DG, Tsirka K, Baltzis D, Paipetis AS. Self-healing materials: A review of advances in materials, evaluation, characterization and monitoring techniques. Compos Part B: Eng 2016;87:92–119.
[21] White SR, Sottos NR, Geubelle PH, Moore JS, Kessler MR, Sriram SR, et al. Autonomic healing of polymer composites. Nature 2001;409(6822):794–7.
[22] Brown EN, White SR, Sottos NR. Microcapsule induced toughening in a self-healing polymer composite. J Mater Sci 2004;39(5):1703–10.
[23] Pang JWC, Bond IP. A hollow fibre reinforced polymer composite encompassing self-healing and enhanced damage visibility. Compos Sci Technol 2005;65(11):1791–9.
[24] Trask RS, Williams GJ, Bond IP. Bioinspired self-healing of advanced composite structures using hollow glass fibres. J R Soc Interface 2007;4(13):363–71.
[25] Kousourakis A, Mouritz AP. The effect of self-healing hollow fibres on the mechanical properties of polymer composites. Smart Mater Struct 2010;19:1–9.
[26] Hamilton AR, Sottos NR, White SR. Self-healing of internal damage in synthetic vascular materials. Adv Mater 2010;22:5159–63.
[27] Hamilton AR, Sottos NR, White SR. Pressurized vascular systems for self-healing materials. J R Soc Interface 2012;70(9):1020–8.
[28] Patrick JF, Hart KR, Krull BP, Diesendruck CE, Moore JS, White SR, et al. Continuous self-healing life cycle in vascularized structural composites. Adv Mater 2014;26:4302–8.
[29] Hart KR, Lankford SM, Freund IA, Patrick JF, Krull BP, Wetzel ED, et al. Repeated healing of delamination damage in vascular composites by pressurized delivery of reactive agents. Compos Sci Technol 2017;151:1–9.
[30] Imato K, Nishihara M, Kanehara T, Amamoto Y, Takahara A, Otsuka H. Self-healing of chemical gels cross-linked by diarylbibenzofuranone-based trigger-free dynamic covalent bonds at room temperature. Angew Chem Int Ed 2012;51:1138–42.
[31] Cordier P, Tournilhac F, Soulié-Ziakovic C, Leibler L. Self-healing and thermoreversible rubber from supramolecular assembly. Nature 2008;451(7181):977–80.
[32] Cooper CB, Root SE, Michalek L, Wu S, Lai J-C, Khatib M, et al. Autonomous alignment and healing in multilayer soft electronics using immiscible dynamic polymers. Science 2023;380:935–41.
[33] Hayes SA, Jones FR, Marshiya K, Zhang W. A self-healing thermosetting composite material. Compos Part A: Appl Sci Manuf 2013;38(4):1116–20.
[34] Meure S, Wu D-Y, Furman SA. FTIR study of bonding between a thermoplastic healing agent and a mendable epoxy resin. Vib Spectrosc 2010;52(1):10–5.
[35] Meure S, Varley RJ, Wu DY, Mayo S, Nairn K, Furman S. Confirmation of the healing mechanism in a mendable EMAA–epoxy resin. Eur Polym J 2012;48(3):524–31.
[36] Pingkarawat K, Dell'Olio C, Varley RJ, Mouritz AP. Poly(ethylene- co - methacrylic acid) (EMAA) as an efficient healing agent for high performance epoxy networks using diglycidyl ether of bisphenol a (DGEBA). Polymer 2016;92:153–63.
[37] Varley RJ, Charve F. EMAA as a healing agent for mendable high temperature epoxy amine thermosets. Compos Part A: Appl Sci Manuf 2012;43(7):1073–80.
[38] Varley RJ, Parn GP. Thermally activated healing in a mendable resin using a non woven EMAA fabric. Compos Sci Technol 2012;72(3):453–60.
[39] Meure S, Furman S, Khor S. Poly[ethylene-co-(methacrylic acid)] healing agents for mendable carbon fiber laminates. Macromol Mater Eng 2010;295(5):420–4.
[40] Pingkarawat K, Bhat T, Craze DA, Wang CH, Varley RJ, Mouritz AP. Healing of carbon fibre–epoxy composites using thermoplastic additives. Polym Chem 2013;4(18):5007–15.
[41] Pingkarawat K, Dell'Olio C, Varley RJ, Mouritz AP. An efficient healing agent for high temperature epoxy composites based upon tetra-glycidyl diamino diphenyl methane. Compos Part A: Appl Sci Manuf 2015;78:201–10.
[42] Wang CH, Sidhu K, Yang T, Zhang J, Shanks R. Interlayer self-healing and toughening of carbon fibre/epoxy composites using copolymer films. Compos Part A: Appl Sci Manuf 2012;43(3):512–8.
[43] Yang T, Du Y, Li ZM, Wang CH. Mechanical properties of self-healing carbon fiber-epoxy composite stitched with mendable polymer fiber. Polym Polym Compos 2014;22(3):329–36.
[44] Ladani RB, Pingkarawat K, Nguyen ATT, Wang CH, Mouritz AP. Delamination toughening and healing performance of woven composites with hybrid z-fibre reinforcement. Compos Part A: Appl Sci Manuf 2018;110:258–67.
[45] Loh TW, Ladani RB, Orifici A, Kandare E. Ultra-tough and in-situ repairable carbon/epoxy composite with EMAA. Compos Part A: Appl Sci Manuf 2021;143:1–10.
[46] Gao Y, Liu L, Wu Z, Zhong Z. Toughening and self-healing fiber-reinforced polymer composites using carbon nanotube modified poly (ethylene-co-methacrylic acid) sandwich membrane. Compos Part A: Appl Sci Manuf 2019;124:105510.
[47] Snyder AD, Turicek JS, Diesendruck CE, Varley RJ, Patrick JF. Unraveling chemical and rheological mechanisms of self-healing with EMAA thermoplastics in fiber-reinforced epoxy composites. Compos Part A: Appl Sci Manuf 2024;185:108271.
[48] Azevedo do Nascimento A, Fernandez F, S. da Silva F, Ferreira EP, Melo JDD, Cysne Barbosa AP. Addition of poly (ethylene-co-methacrylic acid) (EMAA) as self-healing agent to carbon-epoxy composites. Compos Part A: Appl Sci Manuf 2020;137:106016.
[49] Hargou K, Pingkarawat K, Mouritz AP, Wang CH. Ultrasonic activation of mendable polymer for self-healing carbon–epoxy laminates. Compos Part B: Eng 2013;45:1031–9.
[50] Yang T, Zhang J, Mouritz AP, Wang CH. Healing of carbon fibre–epoxy composite T-joints using mendable polymer fibre stitching. Compos Part B: Eng 2013;45:1499–507.
[51] Turicek JS, Snyder AD, Nakshatrala KB, Patrick JF. Topological effects of 3D-printed copolymer interlayers on toughening and in situ self-healing in laminated fiber-composites. Compos Sci Technol 2023;240:110073.
[52] Daniel IM. Engineering mechanics of composite materials. 2nd ed. Oxford University Press; 2006.
[53] Whitney JM, Browning CE. Materials characterization for matrix-dominated failure modes. Eff Defects Compos Mater 1984;104–24.
[54] Hull D. Matrix-dominated properties of polymer matrix composite materials. Mater Sci Eng: A 1994;184(2):173–83.
[55] Sullivan JL, Van Oene H. An elasticity analysis for the generally and specially orthotropic beams subjected to concentrated loads. Compos Sci Technol 1986;27(2):133–55.
[56] Berg CA, Tirosh J, Israeli M. Analysis of short beam bending of fiber reinforced composites. In: Composite materials: Testing and design (second conference). ASTM International; 1972, p. 206–18.
[57] Timoshenko S. On the correction for shear of the differential equation for transverse vibrations of prismatic bars. Lond Edinb Dublin Philos Mag J Sci 1921;41(245):744–6.
[58] Timoshenko S. On the transverse vibration of bars of uniform cross sections. Lond Edinb Dublin Philos Mag J Sci 1922;43(253):125–31.
[59] Elishakoff I. Who developed the so-called Timoshenko beam theory? Math Mech Solids 2020;25(1):97–116.
[60] Wang CM, Reddy JN, Lee KH. Shear deformable beams and plates: Relationships with classical solutions. Amsterdam: Elsevier; 2000.
[61] Reddy JN. Mechanics of laminated composite plates and shells: Theory and analysis. Boca Raton: CRC Press; 2003.
[62] Xie M, Adams DF. Contact finite element modeling of the short beam shear test for composite materials. Comput Struct 1995;57(2):183–91.
[63] Bai SL, Djafari V, Andréani M, François D. In situ study of short-beam shear tests for composite materials. Compos Sci Technol 1995;55(4):343–8.
[64] Wu L, Zhao F, Li Y, Sun X, Liu S, Jiang Q. Progressive damage analysis of three-dimensional hybrid braided composite under short beam shear loading. Compos Struct 2023;313:116960.
[65] Makeev A, He Y, Schreier H. Short-beam shear method for assessment of stress–strain curves for fibre-reinforced polymer matrix composite materials. Strain 2013;49(5):440–50.
[66] Van Der Vossen BC, Makeev AV. Mechanical properties characterization of fiber reinforced composites by nonlinear constitutive parameter optimization in short beam shear specimens. J Compos Mater 2021;55(21):2985–97.
[67] Reddy JN, Miravete A. Practical analysis of composite laminates. CRC Press; 2018.
[68] Rocha I, van der Meer F, Sluys L. Efficient micromechanical analysis of fiber-reinforced composites subjected to cyclic loading through time homogenization and reduced-order modeling. Comput Methods Appl Mech Engrg 2019;345:644–70.
[69] Gopinath G, Batra R. Finite element method based micromechanical methodology for homogenizing fiber/fabrics-reinforced composites and their progressive failure. Compos Struct 2022;286:115279.

[70] Kil T, Bae J-H, Yang B, Lee H-K. Multi-level micromechanics-based homogenization for the prediction of damage behavior of multiscale fiber-reinforced composites. Compos Struct 2023;303:116332.
[71] Kumar A, DasGupta A, Jain A. Microstructure generation algorithm and micromechanics of curved fiber composites with random waviness. Int J Solids Struct 2024;289:112625.
[72] Goudarzi M, Simone A. Discrete inclusion models for reinforced composites: Comparative performance analysis and modeling challenges. Comput Methods Appl Mech Engrg 2019;355:535–57.
[73] Fahmy MA. A new boundary element formulation for modeling and simulation of three-temperature distributions in carbon nanotube fiber reinforced composites with inclusions. Math Methods Appl Sci 2021.
[74] Cui H, Koussios S, Li Y, Beukers A. Measurement of adhesive shear properties by short beam shear test based on higher order beam theory. Int J Adhes Adhes 2013;40:19–30.
[75] Love AEH. A treatise on the mathematical theory of elasticity. 4th ed. Cambridge: Cambridge University Press; 2013.
[76] Toupin RA. Saint-Venant's principle. Arch Ration Mech Anal 1965;18:83–96.
[77] Pagano NJ, Halpin JC. Influence of end constraint in the testing of anisotropic bodies. J Compos Mater 1968;2(1):18–31.
[78] Choi I, Horgan CO. Saint-Venant's principle and end effects in anisotropic elasticity. J Appl Mech 1977;44:424–30.
[79] Horgan CO, Simmonds JG. Saint-Venant end effects in composite structures. Compos Eng 1994;4(3):279–86.
[80] Horgan CO. Recent developments concerning Saint-Venant's principle: An update. Appl Mech Rev 1989;42:295–303.
[81] Horgan CO. On Saint-Venant's principle in plane anisotropic elasticity. J Elasticity 1972;2(3):169–80.
[82] Horgan CO. Some remarks on Saint-Venant's principle for transversely isotropic composites. J Elasticity 1972;2(4):335–9.
[83] J.-J. Luo IMD. Sublaminate-based lamination theory and symmetry properties of textile composite laminates. Compos Part B: Eng 2004;35(6):483–96.
[84] Hashemi S, Kinloch AJ, Williams JG. Corrections needed in double-cantilever beam tests for assessing the interlaminar failure of fibre-composites. J Mater Sci Lett 1989;8:125–9.
[85] Pahr DH, Rammerstorfer FG, Rosenkranz P, Humer K, Weber HW. A study of short-beam-shear and double-lap-shear specimens of glass fabric/epoxy composites. Compos Part B: Eng 2002;33:125–32.